Available online at www.sciencedirect.com

ScienceDirect

Ceramics International 40 (2014) 3003–3009

CERAMICS INTERNATIONAL

www.elsevier.com/locate/ceramint

Nanocrystalline Nd_2O_3: Preparation, phase evolution, and kinetics of thermal decomposition of precursor

Qin Liqin, Wang Kaituo, Wu Xuehang, Wu Wenwei*, Liao Sen, Li Gengming

School of Chemistry and Chemical Engineering, Guangxi University, Nanning 530004, People's Republic of China

Received 20 August 2013; received in revised form 19 September 2013; accepted 1 October 2013
Available online 10 October 2013

Abstract

Nd_2O_3 was synthesized by calcining $Nd_2(C_2O_4)_3 \cdot 10H_2O$ in air. The precursor and its calcined products were characterized by thermogravimetry and differential scanning calorimetry, Fourier transform infrared spectroscopy, X-ray powder diffraction, and scanning electron microscopy. The results showed that high-crystallized Nd_2O_3 with hexagonal structure was obtained when the precursor was calcined at 1223 K in air for 2 h. The crystallite size of Nd_2O_3 synthesized at 1223 K for 2 h was about 48 nm. The thermal decomposition of the precursor in air experienced three steps, which are first, the dehydration of 10 crystal water molecules; then, the decomposition of $Nd_2(C_2O_4)_3$ into $Nd_2O_2CO_3$; and last, the decomposition of $Nd_2O_2CO_3$ into hexagonal Nd_2O_3. Based on the KAS equation, the values of the activation energies associated with the thermal decomposition of $Nd_2(C_2O_4)_3$•$10H_2O$ were determined.

Keywords: Nd_2O_3; Solid-state reaction at low heating temperatures; Non-isothermal kinetics; Thermal decomposition

1. Introduction

Rare earth oxides have many unique properties, such as high mechanical strength, oxygen ion conductivity, oxygen storage capacity, strong UV adsorption, excellent catalysis and luminescence. Therefore, rare earth oxides have been widely used in various fields [1–3]. Among rare earth oxides, neodymium oxide (Nd_2O_3) is kind of very important and has been widely used in photonic applications [4], luminescent and thermoluminescent materials [5,6], protective coatings [7,8], thin films [9], and catalysis [10,11]. The quality of Nd_2O_3 powders was highly dependent on the synthesis method and conditions, which determine particle size and morphology of Nd_2O_3 associated with its performances. Preparations of high-quality samples with superfine particle size and/or dopant have generally been considered to improve the performances of Nd_2O_3 [10,11].

To date, various methods of synthesizing Nd_2O_3 have been developed, including the microemulsion method [1,2], solvothermal synthesis [7], tartrate route [8], the sol–gel method [4,10], the precipitation method [12], the hydrothermal method [13–15], microwave-assisted synthesis [16], combustion process [17], the template method [18], and thermal decomposition of oxalate [19–21]. In the synthesis of Nd_2O_3, it was found that crystallite diameter and morphology of Nd_2O_3 associated with its performances were highly dependent on the synthesis method and conditions. For instance, Yang et al. [10] synthesized single-phase Nd_2O_3 powders with a particle size of 20–30 nm by the sol–gel auto-combustion method using $Nd(NO_3)_3$, citric acid, and polyvinyl alcohol as the starting materials. Phuruangrat et al. [14] obtained pure hexagonal Nd_2O_3 nanorods with about 40 nm in diameter and 100–200 nm long by microwave-assisted hydrothermal reaction, followed by calcination at 773 K for 2 h. Qu et al. [18] obtained Nd_2O_3 nanowires by sol–gel process assisted with porous anodic aluminum oxide as a template. Most researchers attempt to obtain Nd_2O_3 powders with high performance at the lowest possible cost. However, many methods of synthesizing Nd_2O_3 are complex processes with high cost, so it is not easy to prepare the product on a large scale. Therefore, new synthesis methods for hexagonal Nd_2O_3 are needed to be studied and innovated further. Besides, kinetics research of thermal process of Nd_2O_3 precursor still has fewer reports in comparison with synthesis of Nd_2O_3.

This study aimed to prepare monoclinic $Nd_2(C_2O_4)_3$•$10H_2O$ via solid-state reaction at low heating temperatures using Nd $(NO_3)_3 \cdot 5.2H_2O$ and $Na_2C_2O_4$ as raw materials and to study

*Corresponding author. Tel./fax: +86 771 3233718.
E-mail address: gxuwuwenwei@aliyun.com (W. Wenwei).

0272-8842/$ - see front matter © 2013 Elsevier Ltd and Techna Group S.r.l. All rights reserved.
http://dx.doi.org/10.1016/j.ceramint.2013.10.007

phase evolution and the kinetics of thermal decomposition of $Nd_2(C_2O_4)_3$•$10H_2O$. The kinetics of thermal decomposition of $Nd_2(C_2O_4)_3$•$10H_2O$ was studied using TG-DSC technique. Non-isothermal kinetics of thermal decomposition of $Nd_2(C_2O_4)_3$•$10H_2O$ was interpreted by the Kissinger–Akahira–Sunose (KAS) equation [22–27]. The kinetic parameters (E_a, A) and mechanisms of thermal decomposition of $Nd_2(C_2O_4)_3$•$10H_2O$ were discussed.

2. Experimental

2.1. Reagent and apparatus

All the chemicals were of reagent-grade purity (purity > 99.9%). TG/DSC measurements were taken using a Netzsch Sta 409 PC/PG thermogravimetric analyzer under a continuous flow of air (40 mL min^{-1}) and sample mass was around 13 mg. X-ray powder diffraction (XRD) was performed using a Rigaku D/Max 2500 V diffractometer equipped with a graphite monochromator and a Cu target. The radiation applied was Cu Kα (λ=0.15406 nm), operated at 40 kV and 50 mA. The XRD scans were made from 5° to 70° in 2θ with a step size of 0.02°. FT-IR spectra of the precursor and its calcined products were recorded on a Nexus 470 FT-IR instrument. The morphologies of the synthesis products were observed using an S-3400 scanning electron microscope (SEM).

2.2. Preparation of Nd_2O_3

The $Nd_2(C_2O_4)_3$•$10H_2O$ samples were prepared by solid-state reaction at low heating temperatures [22,23] using Nd$(NO_3)_3 \cdot 5.2H_2O$ and $Na_2C_2O_4$ as starting materials. In a typical synthesis, Nd$(NO_3)_3 \cdot 5.2H_2O$ (25.00 g), $Na_2C_2O_4$ (12.45 g), and surfactant polyethylene glycol (PEG)-400 (4.0 mL, 50 vol.%) were placed in a mortar, and the mixture was thoroughly ground by hand with a rubbing mallet for 40 min. The grinding velocity was about 210 cycles/min, and the strength applied was moderate. The reactant mixture gradually became damp, and then a paste was formed quickly. The reaction mixture was kept at 303 K for 1 h. The mixture was washed with deionized water to remove soluble inorganic salts until $C_2O_4^{2-}$ ion could not be visually detected with a 0.5 mol L^{-1} $CaCl_2$ solution. The solid was then washed with a small amount of anhydrous ethanol and dried at 343 K for 8 h. The resulting material was subsequently determined to be $Nd_2(C_2O_4)_3$•$10H_2O$. Hexagonal Nd_2O_3 was obtained via calcining $Nd_2(C_2O_4)_3$•$10H_2O$ at 1223 K in air for 2 h.

3. Method of determining kinetic parameters and mechanism functions

3.1. Determination of activation energy by the KAS equation

Activation energy of thermal decomposition of the solid compound can be obtained by the KAS equation:

$$\ln \frac{\beta}{T^2} = -\frac{E_a}{RT} + \ln \frac{AE_a}{Rg(\alpha)} \quad (1)$$

where β is the heating rate (K min^{-1}), T is the reaction temperature (K) in TG curve, E_a is the activation energy (kJ mol^{-1}) of thermal decomposition, R is the gas constant (8.314×10^{-3} kJ mol^{-1} K^{-1}), A is the pre-exponential factor, and α is called conversion degree.

The conversion degree (α) can be expressed as Eq. (2):

$$\alpha = \frac{m_i - m_t}{m_i - m_f} \quad (2)$$

where m_i, m_f and m_t are the initial, final and current sample masses at the moment t, respectively. The $g(\alpha)$ is a function of α and reveals the mechanism of reaction. The plots of $\ln(\beta/T^2)$ vs. $1/T$ corresponding to different values of α can be obtained by a linear regression of the least-square method. Thus, reaction activation energy E_a can be obtained from linear slope ($-E_a/R$, Eq. (1)).

3.2. Determination of most probable mechanism functions

The following equation was used to estimate the most correct reaction mechanism of thermal decomposition of $Nd_2(C_2O_4)_3$•$10H_2O$, i.e., $g(\alpha)$ function [28–31]:

$$\ln g(\alpha) = \left[\ln \frac{AE_a}{R} + \ln \frac{e^{-x}}{x^2} + \ln h(x)\right] - \ln \beta \quad (3)$$

where x=$E_a/(RT)$, $h(x) = \left(x^4 + 18x^3 + 86x^2 + 96x\right) / \left(x^4 + 20x^3 + 120x^2 + 240x + 120\right)$, and β is the heating rate (K min^{-1}). The conversions α corresponding to multiple rates at the same temperature are put into the left of Eq. (3), combined with 31 types of mechanism functions [29,30,32], the slope k and correlation coefficient r^2 are obtained from the plot of ln $g(\alpha)$ vs. ln β. The probable mechanism function is that for which the value of the slope k is near −1.00000 and correlation coefficient r^2 is better.

3.3. Calculation of pre-exponential factor A

The pre-exponential factor was estimated from the following equation [33]:

$$A = \frac{\beta g(\alpha) E_a}{RT_{max}^2} \exp\left(\frac{E_a}{RT_{max}}\right) \quad (4)$$

where A is the pre-exponential factor (s^{-1}), β is the heating rate (K min^{-1}), $g(\alpha)$ is the most probable mechanism function determined by Eq. (3), E_a is the activation energy (kJ mol^{-1}) of thermal decomposition, R is the gas constant (8.314×10^{-3} kJ mol^{-1} K^{-1}), and T_{max} is the most rapid decomposition temperature (i.e., peak temperature in DTG curve, K).

4. Results and discussion

4.1. TG/DTG/DSC analysis of the precursor

Fig. 1 shows the TG/DTG/DSC curves of the precursor at four heating rates of 5, 10, 15, and 20 K min^{-1} from ambient temperature to 1237 K. The TG/DTG/DSC curves show that thermal process of $Nd_2(C_2O_4)_3$•$10H_2O$ below 1250 K occurs

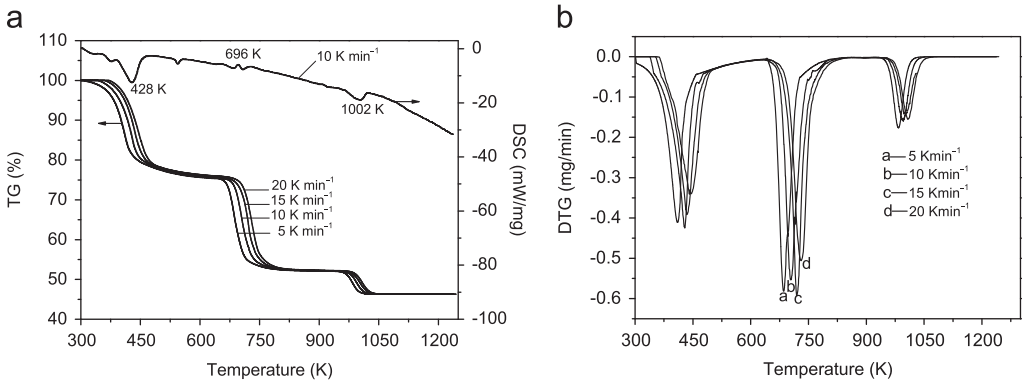

Fig. 1. TG/DTG/DSC curves of $Nd_2(C_2O_4)_3$•$10H_2O$ at different heating rates in air.

in three well-defined steps. For heating rate of 10 K min^{-1}, the first step starts at 336 K, ends at 642 K, which can be attributed to dehydration of the 10 crystal water molecules from $Nd_2(C_2O_4)_3$•$10H_2O$ (mass loss: observed, 24.56%; theoretical, 24.59%). The second decomposition step starts at 642 K, ends at 873 K, attributed to reaction of $Nd_2(C_2O_4)_3$ with $1.5O_2$ molecules into $Nd_2O_2CO_3$, and of the five CO_2 molecules (mass loss: observed, 23.09%; theoretical, 23.48%). The third decomposition step starts at 873 K, ends at 1042 K, attributed to decomposition of $Nd_2O_2CO_3$ into Nd_2O_3, and of the one CO_2 molecule (mass loss: observed, 6.03%; theoretical, 6.01%).

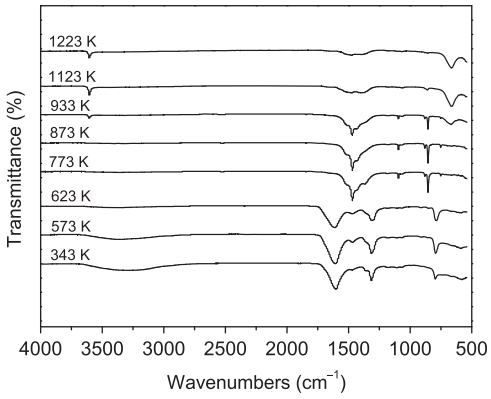

Fig. 2. FT-IR spreactra of $Nd_2(C_2O_4)_3$•$10H_2O$ and its calcined samples.

4.2. IR spectroscopic analysis of $Nd_2(C_2O_4)_3$•$10H_2O$ and its calcined samples

The FT-IR spectra of $Nd_2(C_2O_4)_3$•$10H_2O$ and its calcined samples are shown in Fig. 2. The $Nd_2(C_2O_4)_3$•$10H_2O$ exhibits a broad band at about 3364 cm^{-1} that can be assigned to symmetric and asymmetric stretching modes of water molecules [34–36]. The bending mode of water expected around 1608 cm^{-1} overlaps with the intense oxalate band which is around 1616 cm^{-1} [22,23,37]. The bands at 1313 and 798 cm^{-1} can be assigned to either the appearance of new Nd–OC_2O_3 bonds and/or to the combinations of OH group vibration and lattice modes [37–39]. The weak band at about 1471 cm^{-1} is attributed to ν_{asy} (C=O) from absorption CO_2 [22]. With the increase of the calcination temperature, the bands at about 3364, 1608, 1313, and 798 cm^{-1} become weak and/or disappear. The bands at about 3364, 1607, 1313, and 798 cm^{-1} disappeared when $Nd_2(C_2O_4)_3$•$10H_2O$ was calcined over 1123 K, implying that $Nd_2(C_2O_4)_3$•$10H_2O$ finishes the dehydration and decomposition of $C_2O_4^{2-}$. The spectrum of the calcined sample at 1223 K is in agreement with that of Nd_2O_3 from literature [15].

4.3. XRD analysis of $Nd_2(C_2O_4)_3$•$10H_2O$ and its calcined products

Fig. 3 shows the XRD patterns of $Nd_2(C_2O_4)_3$•$10H_2O$ and its calcined samples. From Fig. 3, the results show that $Nd_2(C_2O_4)_3$•$10H_2O$ is a crystalline compound, all the diffraction peaks in the pattern of sample obtained at 343 K were in agreement with those of monoclinic $Nd_2(C_2O_4)_3$•$10H_2O$, with space group P21/c(14) and the following cell parameters: $a=1.1191$ nm, $b=0.9612$ nm, $c=1.0257$ nm, $\alpha=\beta=90^o$, $\gamma=114.4^\circ$, density = 2.42 g cm^{-3}, from PDF card 20-0764, which indicates that the sample obtained at 343 K is $Nd_2(C_2O_4)_3$•$10H_2O$. When $Nd_2(C_2O_4)_3$•$10H_2O$ was calcined at 773 and 873 K for 2 h, characteristic diffraction peaks of single phase $Nd_2O_2CO_3$ with hexagonal structure in the patterns of two samples appeared. With the increase of the calcination temperature, the characteristic diffraction peaks of $Nd_2O_2CO_3$ become weak and/or disappear. When $Nd_2(C_2O_4)_3$•$10H_2O$ was calcined at 1223 K for 2 h, a new diffraction pattern with strong intensity and smoothed baseline was observed, which indicates that the calcined product had a high degree of crystallinity. Except for a weak diffraction peak of unknown compound at 16.1° for 2θ, all other diffraction peaks in the pattern were in agreement with those of hexagonal Nd_2O_3 with space group P-3m1(164) and the following cell parameters: $a=b=0.383$ nm, $c=0.5999$ nm, $\alpha=\beta=90^o$, $\gamma=120^o$, density = 7.333 g cm^{-3}, from PDF card 41-1089, which indicates that the sample obtained at 1223 K was hexagonal Nd_2O_3.

According to the Scherrer formula [40]: $D=K\lambda/(\beta\cos\theta)$, where D is crystallite diameter, $K=0.89$ (the Scherrer constant), $\lambda=0.15406$ nm (wavelength of the X-ray used), β is the width of line at the half-maximum intensity, and θ is the corresponding angle. The resulting crystallite sizes of the products from calcining precursor at 973, 1123, and 1223 K

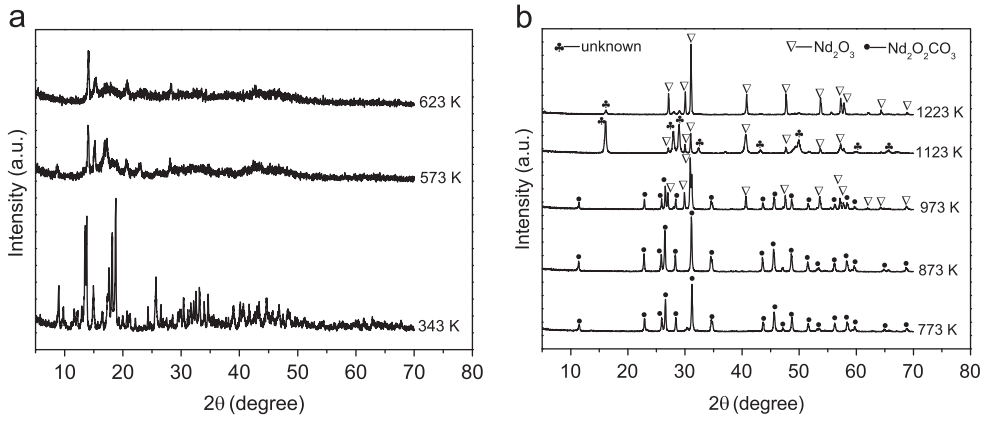

Fig. 3. XRD patterns of $Nd_2(C_2O_4)_3$•$10H_2O$ and its calcined samples at different temperatures for 2 h.

in air for 2 h were 48.5, 29.2, and 48.1 nm, respectively. The crystallinity of hexagonal Nd_2O_3 can be calculated via MDI Jade 5.0 software; the results showed that crystallinities of hexagonal Nd_2O_3 obtained at 973, 1123, and 1223 K were 58.3%, 53.7%, and 93.8%, respectively.

4.4. SEM analyses of $Nd_2(C_2O_4)_3$•$10H_2O$ and its calcined samples

The morphology of $Nd_2(C_2O_4)_3$•$10H_2O$ and its calcined samples are shown in Fig. 4. From Fig. 4a, it can be seen that $Nd_2(C_2O_4)_3$•$10H_2O$ sample is composed of platelets and contains particles having a distribution of small particles (50–250 nm) and large particles (from 250 nm to 1.0 μm). From Fig. 4b–d, the calcined samples obtained at 773, 873, and 973 K are split into approximately spherical particles, and particles sizes are between 50 and 250 nm. With the increase of the calcination temperature, the calcined sample particles are aggregated into larger irregular particles. Fig. 4e and f show the SEM micrographs of samples obtained at 1123 and 1223 K, respectively. It can be seen that the morphology of two samples became irregular shapes, there was a strong soft agglomeration phenomenon among the particles. Average particle diameters of samples obtained at 1123 and 1223 K are about 300 and 1 μm, respectively. The average crystallite sizes of the calcined samples determined by X-ray diffraction were significantly smaller than the values determined by SEM. This can be attributed to the fact that the values observed by the SEM technique have the size of the secondary particles, which were composed of several or many crystallites by soft reunion, and the X-ray line broadening analysis disclosed only the size of a single crystallite.

4.5. Kinetics of thermal decomposition of $Nd_2(C_2O_4)_3$•$10H_2O$

In accordance with TG/DTG/DSC, IR, and XRD analyses of the precursor and its calcined products mentioned above, thermal decomposition of the precursor below 1223 K consists of three steps, which can be expressed as follows.

$$Nd_2(C_2O_4)_3 \cdot 10H_2O\ (s) \rightarrow Nd_2(C_2O_4)_3(s) + 10H_2O\ (s) \quad (5)$$

$$Nd_2(C_2O_4)_3\ (s) + 1.5O_2(g) \rightarrow Nd_2O_2CO_3(h) + 5CO_2(g) \quad (6)$$

$$Nd_2O_2CO_3(h) \rightarrow Nd_2O_3\ (h) + CO_2(g) \quad (7)$$

According to non-isothermal method, the basic data of α and T were collected from the TG curves of thermal decomposition of $Nd_2(C_2O_4)_3$•$10H_2O$ at four heating rates (5, 10, 15, and 20 K min^{-1}). According to Eq. (1), the isoconversional calculation procedure of KAS equation was used. The corresponding KAS lines for different decomposition steps were obtained at different conversion degrees α and different heating rates β at first, and then reaction activation energy E_a can be obtained from linear slope ($-E_a/R$). The results are shown in Fig. 5. From Fig. 5, the average values of the activation energy associated with thermal decomposition of $Nd_2(C_2O_4)_3$•$10H_2O$ were 67.94 ± 143.31, 135.49 ± 13.16, and 453.42 ± 44.78 kJ mol^{-1} for the first, second, and third thermal decomposition steps, respectively.

The activation energy changes of the step 1 with α are higher than 10%, and those of steps 2 and 3 with α are lower than 10%, so we draw a conclusion that dehydration of the ten crystal water molecules from $Nd_2(C_2O_4)_3$•$10H_2O$ could be multi-step reaction mechanisms (step 1); and reaction of $Nd_2(C_2O_4)_3$ with $1.5O_2$ molecules into $Nd_2O_2CO_3$ and CO_2 (step 2), decomposition of $Nd_2O_2CO_3$ into Nd_2O_3 and CO_2 (step 3), are simple reaction mechanisms [29,41–43]. The activation energy of step 3 is higher than those of steps 1 and 2, which implies that the step 3 of thermal decomposition of $Nd_2(C_2O_4)_3$•$10H_2O$ may be interpreted as a "slow" stage, while other steps may be interpreted as "fast" stages.

Fig. 6 shows the curves of α vs. reaction time (t) and $d\alpha/dt$ vs. reaction time (t) for steps 2 and 3. From Fig. 6, steps 2 and 3 are sigmoidal model (sometimes also called autocatalytic) [33,43], which represents the process of steps 2 and 3 whose initial and final stages demonstrate the accelerating and decelerating behavior, respectively, so that the process rate reaches its maximum at some values of the extent of conversion. The results show that rates for steps 2 and 3 reach its maximum at 5.23 and 12.38 min, respectively.

We randomly choose several temperatures which correspond to conversions $0.10 < \alpha < 0.90$ at first, then conversions corresponding to temperature for β=5, 10, 15, and 20 K min^{-1}

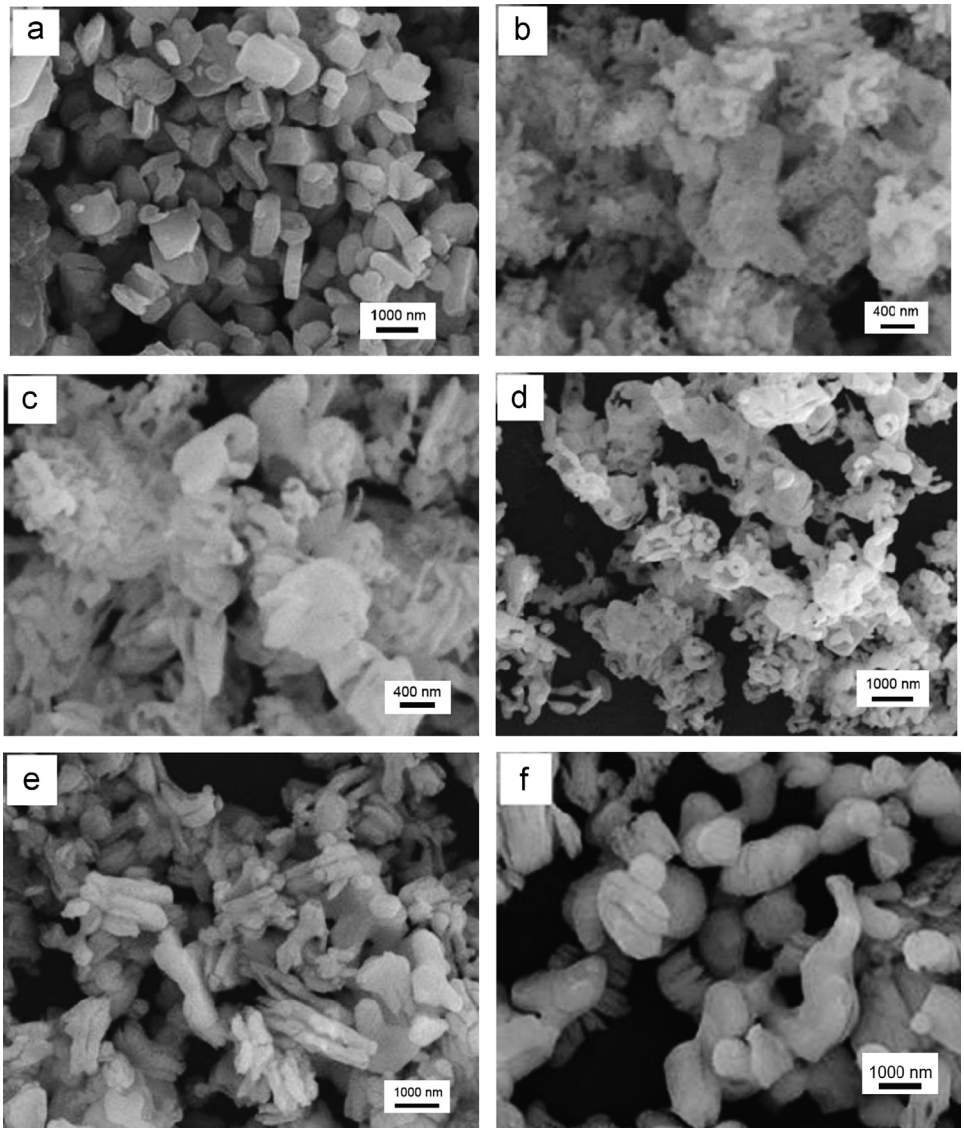

Fig. 4. SEM micrographs of $Nd_2(C_2O_4)_3$•$10H_2O$ and its calcined samples:(a) 343 K, (b) 773 K, (c) 873 K, (d) 973 K, (e) 1123 K, and (f) 1223 K.

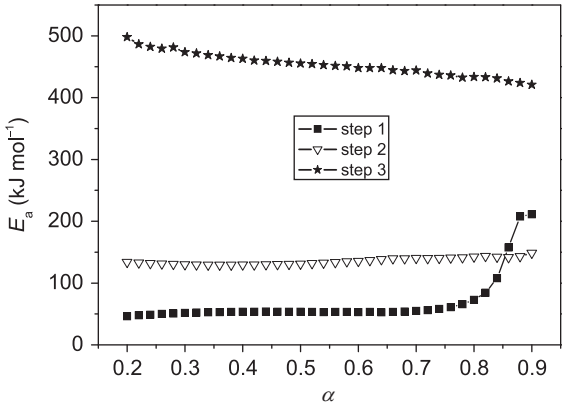

Fig. 5. The dependence of E_a on α at different thermal decomposition steps.

were put into 31 types of mechanism functions [29,30,32]. The slope k, correlation coefficient r^2, and intercept B of linear regression of ln $g(\alpha)$ vs. ln β were obtained. The two mechanism functions of better correlation coefficient r^2 were determined to be probable mechanism functions at first, and then several temperatures were randomly chosen to calculate the slope k, correlation coefficient r^2, and intercept B of the two probable mechanism functions by the same method. Mechanism function in which the value of k is the closest to –1.00000 and the correlation coefficient r^2 is higher is chosen as mechanism function of thermal decomposition of $Nd_2(C_2O_4)_3$•$10H_2O$. The results showed that probable mechanism function integral forms of thermal decomposition of $Nd_2(C_2O_4)_3$•$10H_2O$ for steps 2 and 3 were determined to be $g(\alpha)=[-\ln(1-\alpha)]^{2/3}$ for step 2 and $g(\alpha)=-\ln(1-\alpha)$ for step 3. Rate-determining mechanisms for steps 2 and 3 are assumed random nucleation and its subsequent growth.

The pre-exponential factor was obtained from Eq. (4), inserting the most probable mechanism function $g(\alpha)$, β, E_a, R, and T_{max} values. The results showed that the pre-exponential factors (A) of thermal decomposition of $Nd_2(C_2O_4)_3$•$10H_2O$ for steps 2 and 3 were determined to be 8.75×10^7 and 9.97×10^{22} s^{-1}, respectively.

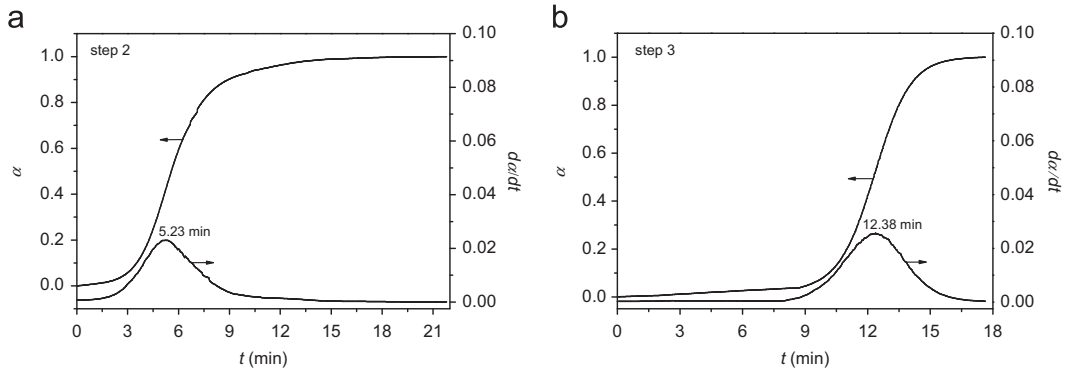

Fig. 6. Curves of α vs. t and $d\alpha/dt$ vs. t at heating rate of 10 K min^{-1}.

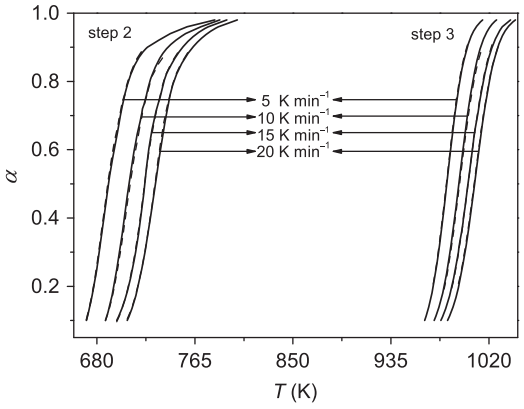

Fig. 7. Comparison of model results (solid line) with the experimental data (dash line) of the thermal decomposition of $Nd_2(C_2O_4)_3$•$10H_2O$ for steps 2 and 3 at different heating rates.

In order to prove the validity of the kinetic mechanisms for steps 2 and 3 of thermal decomposition of $Nd_2(C_2O_4)_3$•$10H_2O$, the comparisons were drawn between experimental data and results of the kinetic mechanism for every heating rate. The results are shown in Fig. 7. It can be found that the model-predicted plots were in agreement with the experimental plots, indicating that the mechanism functions for steps 2 and 3 of thermal decomposition of $Nd_2(C_2O_4)_3$•$10H_2O$ are reliable.

5. Conclusions

We have successfully synthesized hexagonal Nd_2O_3 via calcining $Nd_2(C_2O_4)_3$•$10H_2O$ in air. XRD analysis suggests that high-crystallized Nd_2O_3 with hexagonal structure can be obtained via calcining $Nd_2(C_2O_4)_3$•$10H_2O$ at 1223 K in air for 2 h. The crystallite size of Nd_2O_3 synthesized at 1223 K for 2 h was about 48 nm. The thermal decomposition of $Nd_2(C_2O_4)_3$•$10H_2O$ in air experienced three steps, which involve the dehydration of the 10 crystal water molecules at first, then the reaction of $Nd_2(C_2O_4)_3$ with O_2 into $Nd_2O_2CO_3$, and lastly the decomposition of $Nd_2O_2CO_3$ into hexagonal Nd_2O_3. The average values of activation energy associated with the thermal decomposition of $Nd_2(C_2O_4)_3$•$10H_2O$ were determined to be 67.94 ± 143.31, 135.49 ± 13.16, and 453.42 ± 44.78 kJ mol^{-1} for the first, second, and third thermal decomposition steps, respectively. Thermal decomposition of $Nd_2(C_2O_4)_3$•$10H_2O$ for step 1 could be multi-step reaction mechanisms, and those for steps 2 and 3 were simple reaction mechanisms.

Acknowledgments

This study was financially supported by the National Nature Science Foundation of China (Grant no. 21161002) and the Guangxi Nature Science Foundation of China (Grant no. 2011GXNSFA018036).

References

[1] W.Q. Zhu, J. Ma, L. Xu, W.Z. Zhang, Y.S. Chen, Controlled synthesis of $Nd(OH)_3$ and Nd_2O_3 nanoparticles by microemulsion method, Mater. Chem. Phys. 122 (2010) 362–367.
[2] A. Hadi, I.I. Yaacob, Novel synthesis of nanocrystalline CeO_2 by mechanochemical and water-in-oil microemulsion methods, Mater. Lett. 61 (2007) 93–96.
[3] Z.S. Xiao, B. Zhou, F. Xu, F. Zhu, L. Yan, F. Zhang, A.P. Huang, Energy transfer among rare earth ions induced by annealing process of TmEr codoped aluminum oxide thin films, Phys. Lett. A 373 (2009) 890–893.
[4] T. Sreethawong, S. Chavadej, S. Ngamsinlapasathian, S. Yoshikawa, Sol–gel synthesis of mesoporous assembly of Nd_2O_3 nanocrystals with the aid of structure-directing surfactant, Solid State Sci. 10 (2008) 20–25.
[5] R. Bazzi, M.A. Flores-Gonzalez, C. Louis, K. Lebbou, C. Dujardin, A. Brenier, W. Zhang, O. Tillement, E. Bernstein, P. Perriat, Synthesis and luminescent properties of sub-5-nm lanthanide oxides nanoparticles, J. Lumin. 102–103 (2003) 445–450.
[6] C. Soliman, Neodymium oxide: a new thermoluminescent material for gamma dosimetry, Nucl. Instrum. Methods Phys. Res. Sect. B 251 (2006) 441–444.
[7] M. Zawadzki, L. Kępiński, Synthesis and characterization of neodymium oxide nanoparticles, J. Alloys Compd. 380 (2004) 255–259.
[8] B. Zhaorigetu, R.D. Ga, M. Li, Preparation of Nd_2O_3 nanoparticles by tartrate route, J. Alloys Compd. 427 (2007) 235–237.
[9] A. Kosola, J. Päiväsaari, M. Putkonen, L. Niinistö, Neodymium oxide and neodymium aluminate thin films by atomic layer deposition, Thin Solid Films 479 (2005) 152–159.
[10] W. Yang, Y.L. Qi, Y.J. Ma, X. Li, X.J. Guo, J.Z. Gao, M. Chen, Synthesis of Nd_2O_3 nanopowders by sol–gel auto-combustion and their catalytic esterification activity, Mater. Chem. Phys. 84 (2004) 52–57.
[11] D.G. Filkova, L.A. Petrov, M.Yu. Sinev, Y.P. Tyulenin, Effect of the method of preparation of a Nd_2O_3–MgO catalyst on its efficiency in the reaction of oxidative coupling of methane, Catal. Lett. 13 (1992) 323–329.
[12] S. Liu, R.J. Ma, R.Y. Jiang, F.C. Luo, Synthesis and structure of hydrated neodymium carbonate, J. Cryst. Growth 203 (1999) 454–457.

[13] L. Kępiński, M. Zawadzki, W. Miśta, Hydrothermal synthesis of precursors of neodymium oxide nanoparticles, Solid State Sci. 6 (2004) 1327–1336.
[14] A. Phuruangrat, S. Thongtem, T. Thongtem, Template-free synthesis of neodymium hydroxide nanorods by microwave-assisted hydrothermal process, and of neodymium oxide nanorods by thermal decomposition, Ceram. Int. 38 (2012) 4075–4079.
[15] B. Umesh, B. Eraiah, H. Nagabhushana, B.N. Nagabhushana, G. Nagaraja, C. Shivakumara, R.P.S. Chakradhar, Synthesis and characterization of spherical and rod like nanocrystalline Nd_2O_3 phosphors, J. Alloys Compd. 509 (2011) 1146–1151.
[16] M. Zawadzki, Microwave-assisted synthesis and characterization of ultrafine neodymium oxide particles, J. Alloys Compd. 451 (2008) 297–300.
[17] B.A.A. Balboul, A.Y.Z. Myhoub, The characterization of the formation course of neodymium oxide from different precursors: a study of thermal decomposition and combustion processes, J. Anal. Appl. Pyrolysis 89 (2010) 95–101.
[18] X.F. Qu, J.H. Dai, J.T. Tian, X. Huang, Z.F. Liu, Z.L. Shen, P.P. Wang, Syntheses of Nd_2O_3 nanowires through sol–gel process assisted with porous anodic aluminum oxide (AAO) template, J. Alloys Compd. 469 (2009) 332–335.
[19] L.D. Almeida, S. Grandjean, N. Vigier, F. Patisson, Insights into the thermal decomposition of lanthanide(III) and actinide(III) oxalates–from neodymium and cerium to plutonium, Eur. J. Inorg. Chem. 2012 (2012) 4986–4999.
[20] G.L. Jeyaraj, J.E. House Jr, Thermal studies on yttrium, neodymium and holmium oxalates, Thermochim. Acta 71 (1983) 345–350.
[21] S.S. Moosath, J. Abraham, T.V. Swaminathan, Thermal decomposition of rare earth metal oxalates. I. Oxalates of lanthanum, praseodymium and neodymium, Z. Anorg. Allg. Chem. 324 (1963) 90–95.
[22] X.H. Wu, K.W. Zhou, W.W. Wu, X.M. Cui, Y.N. Li, Magnetic properties of nanocrystalline $CuFe_2O_4$ and kinetics of thermal decomposition of precursor, J. Therm. Anal. Calorimetry 114 (2013) 205–212.
[23] W.W. Wu, Y.N. Li, K.W. Zhou, X.H. Wu, S. Liao, Q. Wang, Nanocrystalline $Zn_{0.5}Ni_{0.5}Fe_2O_4$: Preparation and kinetics of thermal process of precursor, J. Therm. Anal. Calorimetry 110 (2012) 1143–1151.
[24] K. Chrissafis, Kinetics of thermal degradation of polymers, J. Therm. Anal. Calorimetry 95 (2009) 273–283.
[25] X.H. Wu, W.W. Wu, K.W. Zhou, L.Q. Qin, S. Liao, Y.J. Lin, Magnetic nanocrystalline $Mg_{0.5}Zn_{0.5}Fe_2O_4$: preparation, morphology evolution, and kinetics of thermal decomposition of precursor, J. Supercond. Novel Magn., 10.1007/s10948-013-2297-y.
[26] B. Boonchom, Kinetics and thermodynamic properties of the thermal decomposition of manganese dihydrogenphosphate dihydrate, J. Chem. Eng. Data 53 (2008) 1533–1538.
[27] B. Boonchom, N. Vittayakorn, Dehydration Behavior of Synthetic $Al_{0.5}Fe_{0.5}PO_4 \cdot 2.5H_2O$, J. Chem. Eng. Data 55 (2010) 3307–3311.
[28] K.W. Zhou, W.W. Wu, Y.N. Li, X.H. Wu, S. Liao, Preparation of magnetic nanocrystalline $Mn_{0.5}Mg_{0.5}Fe_2O_4$ and kinetics of thermal decomposition of precursor, J. Therm. Anal. Calorimetry 114 (2013) 205–212.
[29] L. Vlaev, N. Nedelchev, K. Gyurova, M. Zagorcheva, A comparative study of non-isothermal kinetics of decomposition of calcium oxalate monohydrate, J. Anal. Appl. Pyrolysis 81 (2008) 253–262.
[30] L. Liqing, C. Donghua, Application of iso-temperature method of multiple rate to kinetic analysis: dehydration for calcium oxalate monohydrate, J. Therm. Anal. Calorimetry 78 (2004) 283–293.
[31] Z.P. Chen, Q. Chai, S. Liao, X. Chen, Y. He, Y. Li, W.W. Wu, B. Li, Nonisothermal kinetic study: IV. Comparative methods to evaluate Ea for thermal decomposition of $KZn_2(PO_4)(HPO_4)$ synthesized by a simple route, Ind. Eng. Chem. Res. 51 (2012) 8985–8991.
[32] H.Y. Jiang, J.G. Wang, S.Q. Wu, B.S. Wang, Z.Z. Wang, Pyrolysis kinetics of phenol–formaldehyde resin by non-isothermal thermogravimetry, Carbon 48 (2010) 352–358.
[33] S. Vyazovkin, A.K. Burnham, J.M. Criado, L.A. Pérez-Maqueda, C. Popescu, N. Sbirrazzuoli, ICTAC kinetics committee recommendations for performing kinetic computations on thermal analysis data, Thermochim. Acta 520 (2011) 1–19.
[34] B. Boonchom, N. Vittayakorn, Simple fabrication of polyhedral grain-like microparticle $Cu_{0.5}Zn_{0.5}HPO_4 \cdot H_2O$ and porous structure CuZnP2O7, Ceram. Int. 38 (2012) 411–415.
[35] Z.G. Jian, D.P. Ren, Q.Z. Wang, L.X. Xu, R.S. Zhu, Structural and magnetic properties of $Co_{1-x}Zn_xFe_2O_4$ nanorods prepared by the solvothermal annealing method, Ceram. Int. 39 (2013) 6113–6118.
[36] I. Uysal, F. Severcana, Z. Evis, Characterization by Fourier transform infrared spectroscopy of hydroxyapatite co-doped with zinc and fluoride, Ceram. Int. 39 (2013) 7727–7733.
[37] X.H. Wu, W.W. Wu, K.W. Zhou, X.M. Cui, S. Liao, Products and nonisothermal kinetics of thermal decomposition of $MgFe_2(C_2O_4)_3 \cdot 6H_2O$, J. Therm. Anal. Calorimetry 110 (2012) 781–787.
[38] N. Deb, Some heterobimetallic oxalate coordination precursors of lanthanum(III) of the type, $M_3[La(C_2O_4)_3(H_2O)_m]_2 \cdot nH_2O$ (M=Mn(II), Co(II), Ni(II) and Cu(II)) 107 (2012) 561–571J. Therm. Anal. Calorimetry 107 (2012) 561–571.
[39] M.A. Gabal, S.A.K. Elroby, A.Y. Obaid, Synthesis and characterization of nano-sized ceria powder via oxalate decomposition route, Powder Technol. 229 (2012) 112–118.
[40] K.W. Zhou, X.H. Wu, W.W. Wu, J. Xie, S.Q. Tang, S. Liao, Nanocrystalline $LaFeO_3$ preparation and thermal process of precursor, Adv. Powder Technol. 24 (2013) 359–363.
[41] P. Budrugeac, V. Muşat, E. Segal, Non-isothermal kinetic study on the decomposition of Zn acetate-based sol–gel precursor, J. Therm. Anal. Calorimetry 88 (2007) 699–702.
[42] N. Chaiyo, R. Muanghlua, S. Niemcharoen, B. Boonchom, P. Seeharaj, N. Vittayakorn, Non-isothermal kinetics of the thermal decomposition of sodium oxalate $Na_2C_2O_4$, J. Therm. Anal. Calorimetry 107 (2012) 1023–1029.
[43] W.W. Wu, K.T. Wang, Y.N. Li, X.H. Wu, S. Liao, Q. Wang, Nanocrystalline $LiMn_2O_4$ preparation and kinetics of thermal process of precursor, J. Therm. Anal. Calorimetry 112 (2013) 1391–1399.